Energy Advances

ROYAL SOCIETY OF CHEMISTRY

PAPER

View Article Online
View Journal

Cite this: DOI: 10.1039/d5ya00362h

Engineering Al/Fe dual-doped nanoporous ZnO nanorods for efficient visible-light-driven photoelectrochemical hydrogen evolution

Mustafa Majid Rashak Al-Fartoos, *[a] Asif Ali Tahir [a] and Martin Smith[b]

Received 11th December 2025,
Accepted 8th June 2026

DOI: 10.1039/d5ya00362h

rsc.li/energy-advances

The transition toward sustainable energy systems has increased interest in solar driven photoelectrochemical hydrogen generation. Among available photoanodes, ZnO is attractive for its abundance and favourable charge transport properties, yet its performance remains restricted by poor visible light absorption and rapid charge recombination. Although doping and nanorod engineering have been widely explored, the combined use of Al/Fe dual doping with a nanoporous ZnO nanorod architecture remains underexplored. Here, we fabricate nanoporous ZnO nanorods modified through synergistic Al and Fe co-doping. Al^{3+} enhances carrier density and conductivity, while Fe^{3+} introduces beneficial sub-bandgap states and drives the formation of a highly nanoporous surface, expanding the electroactive area and improving charge separation. The resulting photoanodes exhibit significantly enhanced PEC hydrogen evolution performance compared to pristine ZnO, achieving a photocurrent density of 3 mA cm^{-2} at 1 V *vs.* RHE, reduced charge-transfer resistance, and long-term operational stability over 5 h under sacrificial Na_2SO_3 electrolyte conditions. Electrolyte-dependent tests further confirmed the strong influence of pH and sacrificial agents on PEC performance, and among electrolytes, Na_2SO_3 provides the best stability. Furthermore, the electrode demonstrates stable visible-light-driven hydrogen generation, producing 5.7 mL cm^{-2} of H_2 over 5 hours.

1. Introduction

In 2022, the global population reached 8 billion and is projected to rise to 10 billion by 2050, placing unprecedented demands on global energy infrastructures.[1] This population growth will significantly increase energy requirements, with global energy consumption expected to rise by more than 50% by 2050.[2] Continued reliance on fossil fuels will exacerbate greenhouse gas emissions and intensify the impacts of climate change, including extreme weather events, sea-level rise, and environmental degradation.[3] Given the increasing severity and magnitude of these impacts, there is an urgent global need to transition towards carbon-free energy systems and accelerate the integration of renewable energy sources.

Among the most promising alternatives is hydrogen energy, a clean, high energy density carrier with the potential to decarbonize hard to electrify sectors such as heavy industry, transport, and long-duration energy storage. Hydrogen can be produced in various forms, including grey hydrogen (from natural gas), blue hydrogen (from natural gas with carbon capture and storage), and pink hydrogen (from nuclear powered electrolysis).[4] However, these pathways either release CO_2 or require significant energy inputs.[5] By contrast, green hydrogen, produced *via* renewable energy powered electrolysis, is considered the cleanest and most sustainable option, as it generates zero direct carbon emissions.[5]

To be sustainable, hydrogen must be produced through fossil-free pathways. Photoelectrochemical (PEC) hydrogen generation has been identified as a promising method, as it harnesses solar energy to directly split water into hydrogen and oxygen, thereby integrating solar energy conversion with chemical energy storage.[6] Recent studies demonstrate the potential of scalable solar hydrogen production as a key contributor to global climate goals by enabling sustainable transport, industrial processes, and clean power generation.[7] However, achieving efficient PEC hydrogen production requires the development of robust photoelectrode materials capable of effectively harvesting sunlight and driving hydrogen evolution reactions.[8,9]

TiO_2, Fe_2O_3, and $BiVO_4$ are well-known and widely studied photoanodes for photoelectrochemical (PEC) hydrogen evolution.[10,11] TiO_2, although highly stable in aqueous media, possesses a wide bandgap ($\sim$3.2 eV) that restricts absorption to the UV region, leading to low solar to hydrogen conversion efficiencies $<$1%.[12] Fe_2O_3 offers visible-light absorption due to its narrower bandgap ($\sim$2.1 eV); however, its poor electrical conductivity, short hole diffusion length, and sluggish surface

[a] Solar Energy Research Group, Environment and Sustainability Institute, University of Exeter, Penryn Campus, Cornwall TR10 9FE, UK. E-mail: ma994@exeter.ac.uk
[b] School of Applied Sciences, University of Brighton, Brighton, UK

reaction kinetics limit the achievable photocurrent density to ~2–3 mA cm^{-2} under standard illumination.[12] $BiVO_4$, with a bandgap of ~2.4 eV, shows enhanced visible-light harvesting and a higher theoretical photocurrent (~7 mA cm^{-2}), but it continues to suffer from low electron mobility, moderate photostability, and reliance on relatively scarce elements.[13]

On the other hand, zinc oxide (ZnO) has received widespread interest as a photoanode material for photoelectrochemical hydrogen generation owing to its high electron mobility, suitable band-edge alignment for water redox reactions, good chemical stability in the dark, non-toxicity, and cost-effectiveness.[11] Composed of earth-abundant elements, ZnO can be easily synthesized into diverse nanostructured morphologies at low temperatures, making it well-suited for large-scale and cost-effective fabrication.[14] As such, ZnO is considered a promising candidate for the development of PEC systems for solar hydrogen production. However, pristine ZnO suffers from several drawbacks that compromise its PEC performance. Its wide bandgap (3.2–3.3 eV) restricts absorption primarily to the ultraviolet (UV) region, which accounts for only ~5% of the solar spectrum.[15] Moreover, rapid electron–hole recombination and photocorrosion under illumination further reduce its quantum efficiency and long-term stability.[16] These challenges remain major barriers to the practical implementation of ZnO in PEC hydrogen evolution for sustainable solar hydrogen production.

Current research on ZnO photoanodes emphasizes doping, heterostructure design, and morphology engineering to enhance visible light absorption and photoelectrochemical performance. Among these approaches, elemental doping is particularly effective, as it modifies the band structure, electronic properties, and surface chemistry of ZnO. Dopant incorporation introduces additional electronic states and lattice perturbations that reduce the effective bandgap and improve visible-light harvesting compared with pristine ZnO.[17] A wide range of dopants, including Ag, Fe, Al, Cr, Co, Ni, Cu, Pb, and Sb, which can tune its band structure and improve charge separation.[18–22] Rare-earth and noble-metal dopants such as La and Ag further improve performance by increasing carrier density, generating oxygen vacancies (V_O), and enhancing visible-light absorption through bandgap narrowing and plasmonic effects.[22–24]

Fe one of the most promising dopant as it introduces donor states that reduce the bandgap (*e.g.*, from ~3.11 to 2.95 eV) and extend visible-light absorption, enabling a photocurrent density of 4.2 mA cm^{-2} at 1 V *vs.* RHE compared to only 0.25 mA cm^{-2} for pristine ZnO in 1 M Na_2SO_4 solution.[25] Similarly, Al doped ZnO enhances carrier concentration, reduces crystallite size, and promotes preferential *c*-axis orientation, which collectively improve PEC performance and stability.[26] These doping strategies broaden ZnO's visible-light response, enhance charge dynamics, and accelerate interfacial water oxidation kinetics, making doped ZnO a highly promising platform for solar hydrogen production.

Besides chemical doping, morphological engineering of ZnO also plays a critical role in improving PEC water-splitting performance. One-dimensional ZnO nanorods, particularly when vertically aligned on conductive substrates, provide efficient electron transport pathways with minimal grain boundaries, thereby reducing recombination losses.[27] Their high surface area to volume ratio enhances interfacial contact with the electrolyte and improves catalytic activity.[28] Moreover, the elongated geometry of nanorods enables effective light harvesting through reduced reflection and enhanced internal scattering.[29] A further advantage lies in their fabrication: ZnO nanorods can be synthesized by relatively low cost and scalable methods such as hydrothermal growth and electrochemical deposition, in contrast to TiO_2, which often requires more complex processing routes.[11] Additionally, the single crystal nature of ZnO nanorods suppresses defect states, making these architectures structurally and electronically superior platforms for achieving higher PEC efficiencies.[30]

Another effective strategy to enhance PEC performance of ZnO and address intrinsic limitations such as UV constrained absorption and elevated electron hole recombination, is heterostructure engineering. Coupling ZnO with visible light responsive semiconductors like CdS or $BiVO_4$ in core shell or junction architectures broadens light absorption into the visible spectrum and improves charge separation through favourable band alignment and built in electric fields. For instance, a ZnO/CdS heterostructure achieved a photocurrent density of 1.7 mA cm^{-2} at 1 V *vs.* RHE, outperforming pristine ZnO *via* enhanced visible-light capture and efficient interfacial charge transfer.[31] Similarly, a ZnO/$BiVO_4$ heterojunction delivered a photocurrent density of 1.72 mA cm^{-2} at 1.81 V *vs.* RHE, surpassing that of pure ZnO NRs due to reduced recombination and improved spectral response.[32] Furthermore, ZnO/$NiFe_2O_4$ heterojunction nanorod photoanodes achieved photocurrent densities of 1.1 mA cm^{-2} at 1 V *vs.* RHE, compared to only 0.4 mA cm^{-2} for pristine ZnO nanorods, owing to enhanced visible-light harvesting, reduced charge recombination, and improved interfacial charge transfer.[33] Moreover, a recently developed Al doped ZnO nanorod array coated with an ultrathin $FeVO_4$ shell (forming a type-II heterojunction) yielded 1.13 mA cm^{-2} at 1.23 V *vs.* RHE (AM 1.5G) more than double that of the AZO substrate alone thanks to reduced bulk recombination and optimized interfacial charge separation.[34]

Co-doping with two different metal elements has proved a promising method in boosting ZnO's photocatalytic hydrogen evolution activity through expansion of light absorption and inhibition of charge recombination. As an example, hydrothermally prepared Al/Ce co-doped ZnO realized minimized bandgap from 3.37 to 2.64 eV.[35] Correspondingly, solution combustion synthesized Al/Ni co-doped ZnO showed increased donor density due to Al incorporation and Ni-induced mid-gap states, which together extended visible light absorption and reduced recombination.[36] However, photoelectrochemical hydrogen generation imposes fundamentally different requirements, including bias-driven charge transport, favourable band bending at the semiconductor–electrolyte interface, and long-term operational stability—factors that cannot be inferred from photocatalytic performance alone. Despite the progress in photocatalysis, to our knowledge, the dual-doped ZnO as a photoanode for PEC hydrogen evolution remains largely unexplored, highlighting the need to explore co-doping strategies specifically tailored for PEC architectures.

A major limitation of ZnO photocatalysts in water-splitting systems is their intrinsic chemical instability, which makes their long-term performance highly dependent on the choice of electrolyte. In strongly alkaline media (like NaOH or KOH) enhance photocurrent and H_2 production by providing abundant OH^- ions, which catalyse the oxygen-evolution reaction, but at elevated pH ZnO dissolves.[37] Neutral salt electrolytes (like Na_2SO_4 at pH 7) develop mild conditions with moderate photocurrents and reduced initial corrosion, but ZnO continues to photo dissolve gradually as photogenerated holes form localised H^{1+} that leach Zn^{2+} ions from its lattice.[37] In acidic conditions (*e.g.*, in HCl), ZnO photocorrodes rapidly through direct proton attack ($ZnO + 2H^+ \rightarrow Zn^{2+} + H_2O$), leading to extensive dissolution and loss of photocatalytic function.

Special buffer electrolytes, such as borate and carbonate, significantly enhance ZnO's activity and stability: at moderately alkaline pH (9–11), they retain high photocurrents (*e.g.*, 99% initial value after 1 h) and generate protecting layers or intermediates, which inhibit ZnO photocorrosion.[37,38] ZnO nanowire films generated hydrogen in the presence of a Na_2S/Na_2SO_3 sacrificial mixture, which acts as an efficient hole scavenger, achieving a rate of 0.53 μmol cm^{-2} h^{-1} under broadband illumination with excellent stability over 50 h.[38,39] Nevertheless, despite these advantages, the overall PEC performance in these electrolytes remains lower than that achieved in strong alkaline (NaOH) or strongly acidic (HCl) environments, highlighting the challenge of balancing activity with long term ZnO stability.

Despite notable progress, ZnO based photoanodes still suffer from limited visible-light absorption, rapid charge recombination, and insufficient operational stability. In this work, we address these limitations through synergistic Al/Fe dual doping of ZnO nanorod thin films, a strategy that not only tailors the electronic structure but also induces a distinct nanoporous surface architecture. This dopant-driven nanoporosity significantly increases the electroactive area and enhances charge separation and transport. Additionally, electrolyte-dependent studies using NaOH, Na_2SO_3, and other pH-tuned media were performed to optimize interfacial kinetics and operational stability. Our findings reveal that the combination of nanoporosity engineering and dual-dopant modulation, together with tailored electrolyte conditions, significantly enhances photoelectrochemical hydrogen evolution performance compared with pristine ZnO. In the following sections, we detail the synthesis of the nanoporous dual-doped ZnO nanorods, their structural and electrochemical characterization, and the evaluation of their PEC activity under different electrolyte environments.

2. Experiments and methods

2.1 Materials

Zinc nitrate hexahydrate ($Zn(NO_3)_2{\cdot}6H_2O$) was obtained from Fisher Scientific, sodium nitrate ($NaNO_3$) from Acros Organics, hexamethylenetetramine (HMTA, $C_6H_{12}N_4$) and sodium hydroxide (NaOH) from Merck aluminium nitrate nonahydrate ($Al(NO_3)_3{\cdot}9H_2O$), iron nitrate nonahydrate ($Fe(NO_3)_3(H_2O)_9$) sodium sulfite (Na_2SO_3), and sodium sulfide (Na_2S) were purchased from Thermo Scientific. Fluorine-doped tin oxide (FTO) glass substrates (NSG TEC 5) were provided by Pilkington. All chemical reagents were used without further purification, and all solutions were prepared using double-distilled water.

2.2 Preparation of photoanode

Pure and Al-doped ZnO nanorod (NR) films were synthesized on fluorine-doped tin oxide (FTO) glass substrates *via* a standard three-electrode electrochemical deposition system comprising a saturated Ag/AgCl reference electrode, a Pt wire counter electrode, and an FTO working electrode. The deposition was performed from an aqueous solution containing 75 mM $Zn(NO_3)_2{\cdot}6H_2O$, 0.1 M $NaNO_3$, 25 mM hexamethylenetetramine (HMTA), and $Al(NO_3)_3{\cdot}9H_2O$ and $Fe(NO_3)_3{\cdot}9H_2O$ at 0, 1, 5, and 10 mol% relative to $Zn(NO_3)_2{\cdot}6H_2O$. Prior to deposition, the FTO substrates were ultrasonically cleaned in distilled water, ethanol, and acetone, then dried. A two-step potentiostatic deposition process was employed: a brief −1.3 V pulse (*vs.* Ag/AgCl) for 0.5 seconds to create a seed layer, followed by growth at −1.0 V (*vs.* Ag/AgCl) for 1200 s at 80 °C. After electrodeposition, the films were rinsed with deionized water, air dried, and annealed at temperatures up to 500 °C for 1 hour. The growth mechanism involves the electrochemical generation of OH^- ions, which react with Zn^{2+} to form $Zn(OH)_2$ on the cathode surface. Upon heating, $Zn(OH)_2$ dehydrates to form crystalline ZnO. HMTA serves as a pH buffer and a slow releasing source of OH^- ions, controlling ZnO morphology and nanorod alignment through regulated nucleation and growth dynamics. The doping optimization was carried out by systematically varying the Al/Fe co-doping concentrations (0, 1, 5, and 10 mol%) to identify the composition yielding the highest photocurrent density. The optimal performance was achieved at 5 mol% co-doping. Subsequently, corresponding single-doped samples (Al-only and Fe-only) were prepared at the same concentrations to enable direct comparison of individual and synergistic effects. All deposition procedures were conducted using an Autolab PGSTAT30 system controlled *via* NOVA 2.1 software.

2.3 Materials characterization

The structural, morphological, compositional, optical, and photoelectrochemical properties of the synthesized ZnO-based thin films were systematically investigated using a range of characterization techniques. Crystallographic analysis was conducted using a Bruker D8 advance X-ray diffraction (XRD) system. Surface morphology and nanostructural features were examined by scanning electron microscopy (SEM) using an FEI XT Nova NanoLab 600 instrument.

Elemental composition and dopant distribution within the thin-film coatings were examined by energy-dispersive X-ray spectroscopy (EDS) using an Oxford Instruments X-MAXN system integrated with the scanning electron microscope. The micro X-ray fluorescence instrument (μ-XRF analysis was performed using a Bruker M4 Tornado plus μ-XRF mapping system equipped with a micro-focused Rh source (50 kV, 600 μA) with a

poly-capillary optic (25 μm spot-size). The detector of μ-XRF system employed two silicon drift detectors (SDD) to collect fluorescence spectra from the specimen. Optical transparency was assessed using a PerkinElmer UV-vis spectrophotometer. The optical band gap (E_g) of the films was calculated from the absorbance spectra using Tauc's method to determine the nature of the electronic transitions.

X-ray photoelectron spectroscopy (XPS) was performed using an ESCALAB 250Xi spectrometer (Thermo Scientific) with monochromated Al Kα radiation (1486.6 eV). Spectra were acquired in selected area mode (900 μm). Survey scans (1 eV step, 150 eV pass energy) and high-resolution scans (0.1 eV step, 20 eV pass energy) were collected for Fe 2p, Zn 2p, C 1s, and O 1s regions. Data were analyzed using Thermo Avantage (v5.952), with binding energies calibrated to the C 1s peak at 285.0 eV. The FWHM of Fe 2p peaks was constrained between 1.0–1.5 eV.

2.4 Photoelectrochemical performance evaluation

Photoelectrochemical (PEC) measurements were performed using a Metrohm Autolab PGSTAT302N workstation with a three-electrode setup: a platinum wire as the counter electrode, an Ag/AgCl saturated with (3 M KCl) reference electrode, and the FTO coated ZnO-based film as the working electrode. 1 M NaOH, 0.1 M Na_2SO_3, 0.1 M (mix of 25% Na_2S, and 75% Na_2SO_3), and 0.5 M Na_2SO_4 aqueous solutions served as the electrolyte. Simulated solar irradiation 1 sun was provided by a Newport 66902 xenon lamp (300 W) equipped with UV filter. Linear sweep voltammetry (LSV) was recorded in the range of −0.3 V to +0.6 V at a scan rate of 10 mV s^{-1}. All measurements were performed under front side illumination with the working electrode area fixed at 1.0 cm^2. The applied potential *vs.* the reversible hydrogen electrode (RHE) was calculated using the Nernst equation:

$$E_{RHE} = E_{Ag/AgCl} + 0.1976 + 0.0591 \times pH \quad (1)$$

Mott–Schottky (M–S) analysis was performed in the dark by recording capacitance voltage characteristics at a fixed frequency of 1 kHz with an AC perturbation of 5–10 mV, sweeping the applied potential from 0 to 1.8 V *vs.* RHE. The resulting $1/C^2$–V plots were used to estimate the flat-band potential (V_{fb}) from the x-intercept and donor carrier density (N_D) from the slope, assuming a dielectric constant of 8.5 for ZnO. Electrochemical impedance spectroscopy (EIS) was also conducted under both dark and illuminated conditions using the same three-electrode configuration. EIS measurements were carried out over a frequency range of 0.1 Hz to 100 kHz with an AC amplitude of 10 mV at open-circuit potential.

The hydrogen generation rate was evaluated by collecting the evolved gas from the PEC reactor and analysing it using gas chromatography (GC, PerkinElmer Clarus 580) equipped with a thermal conductivity detector (TCD) and a molecular sieve column. Prior to measurement, the GC system was calibrated using standard hydrogen–nitrogen gas mixtures. The experiments were performed under continuous 1 sun illumination for 5 h at an applied potential of 1 V *vs.* RHE, with hydrogen quantified at regular intervals using high-purity N_2 as the carrier gas.

3. Results and discussion

3.1 X-ray diffraction analysis

The crystalline structure of pristine ZnO thin films, Al doped ZnO, Fe doped ZnO, and Al/Fe-doped ZnO was characterized using X-ray diffraction (XRD), as shown in Fig. 1. The diffraction patterns distinctly reveal high intensity peaks corresponding to the crystal planes (100), (002), (101), (102), and (110), all aligned with the hexagonal wurtzite ZnO phase (JCPDS card no. 00-036-1451).[14,40] Importantly, no diffraction peaks indicative of secondary phases, such as metallic Al, Al_2O_3, Fe, or iron oxides, were observed. This absence confirms the effective substitution and incorporation of Al^{3+} and Fe^{3+} ions into the ZnO lattice without the formation of detectable impurities or segregated compounds.

The most intense diffraction peaks across all samples were the (002) and (101) reflections, with the (002) peak signifying a strong preferential growth orientation along the *c*-axis perpendicular to the substrate surface.[41] Upon Al doping, the (002) peak notably shifts to higher diffraction angles, indicating lattice expansion attributed to the replacement of Zn^{2+} ions with Al^{3+} ions, thus confirming successful doping. Introducing Fe as an additional dopant alongside Al further accentuates this shift, clearly highlighting successful dual doping.[42,43]

The intensity of the (002) diffraction peak increases significantly upon doping, doubling with Al incorporation and rising more than twentyfold with Al/Fe co-doping. This enhancement is primarily attributed to improved *c*-axis preferential orientation.[42,43] In electrodeposited ZnO nanorods, the (002) reflection reflects the fraction of crystallites aligned with their *c*-axis normal to the substrate. Al^{3+} promotes anisotropic growth by modifying surface energies and suppressing lateral growth, while Fe^{3+} further influences growth kinetics through lattice strain and defect formation, enhancing vertical alignment when combined with Al.

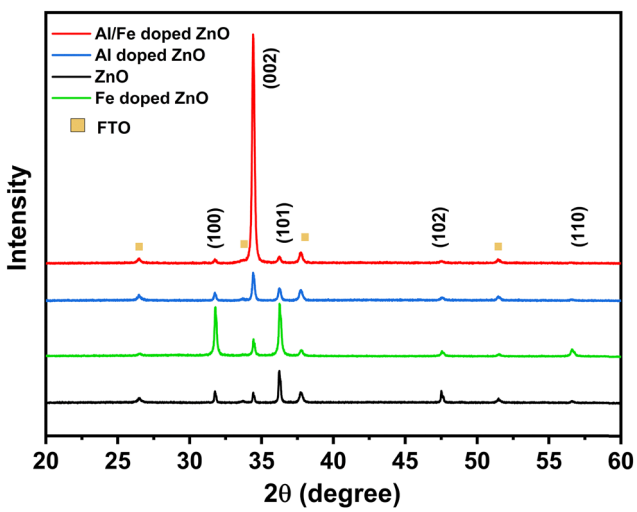

Fig. 1 XRD patterns of pristine ZnO nanorod thin films, Al-doped ZnO, Fe-doped ZnO and Al and Fe doped ZnO, all deposited on FTO substrates.

However, Fe single-doped ZnO does not exhibit dominant (002) orientation, as the (100) and (101) reflections remain predominant, indicating that Fe alone does not induce *c*-axis alignment.[44] Instead, Al is the main driver of anisotropic structural orientation, while Fe primarily affects defect formation and growth kinetics rather than crystal growth direction. Although peak intensity may also vary with film thickness, the strong enhancement of the (002) peak in the co-doped sample supports dopant-induced preferential orientation.[41,42]

Crystallite sizes were estimated using the Scherrer equation:

$$D = \frac{K\lambda}{\beta \cos\theta} \quad (2)$$

where K = 0.9 was used as the shape factor, λ = 1.5406 Å corresponds to Cu Kα radiation, and β represents the full width at half maximum (FWHM). The average crystallite size decreased from 55.91 nm for pristine ZnO to 36.75 nm upon Al doping, and a further slight reduction to approximately 35.14 nm with Al and Fe dual doping. Such reductions reflect restricted crystallite growth due to lattice strain and increased defect density resulting from doping, aligning well with previous studies in the literature.[45,46] Moreover, the simultaneous decrease in crystallite size (increased FWHM) indicates that the (002) peak enhancement arises mainly from improved texture rather than increased crystallinity. Additionally, doping causes an observable increase in lattice constants; specifically, the lattice constant *c* (measured from peak (002)) increased from 5.2063 Å (ZnO) to 5.2078 Å (Al doped ZnO) and further slightly to 5.2079 Å (Al and Fe doped ZnO). Similarly, lattice constant *a* (measured from peak (100)) expanded from 3.250 Å (ZnO) to 3.251 Å for both Al doped ZnO and Al and Fe doped ZnO.

3.2 X-ray photoelectron spectroscopy (XPS)

XPS measurements were performed to investigate the surface chemical composition and electronic structure of ZnO and Fe/Al co-doped ZnO samples. Survey spectra confirm that both surfaces are dominated by Zn and O, with carbon (10.8–13.1 at%) attributed to adventitious carbon and minor carbonate species. Trace chloride is also detected (1.6–1.9 at%). The Fe concentration is low, detected at ~0.6–0.8 at% in Fe/Al co-doped ZnO, while only a very weak signal near the detection limit is observed in pristine ZnO. Aluminium is below the detection limit of XPS (~0.1 at%) in both samples, consistent with its low concentration and in agreement with EDS and μXRF results.

High-resolution C 1s spectra for both samples show a dominant C–C peak at ~284.2–284.4 eV (Fig. 2a and b), consistent with the standard reference (~284.8 eV),[47] confirming negligible surface charging. Additional components corresponding to C–O and carbonate species are observed, indicating the presence of surface-adsorbed carbon species. The presence of carbonate suggests that contributions from surface adsorbates must be considered when interpreting the O 1s spectra.

The O 1s spectra exhibit two main components: a dominant peak at ~530.2 eV attributed to lattice oxygen (O^{2-} in ZnO), and a higher binding energy component at ~531–532 eV (Fig. 2c and d).[48] This secondary peak is commonly associated with defect-related oxygen species, including surface hydroxyl groups, carbonate species, and possible oxygen vacancies.[49,50] However, due to the overlap of contributions from carbonate species and other surface adsorbates, XPS alone cannot unambiguously distinguish or quantify oxygen vacancies.[50]

The Zn $2p_{3/2}$ peak is observed at ~1020.4 eV for ZnO and shifts to ~1021.5 eV for Fe/Al co-doped ZnO, consistent with Zn^{2+} in ZnO (Fig. 2e and f).[48] The slight positive shift in the

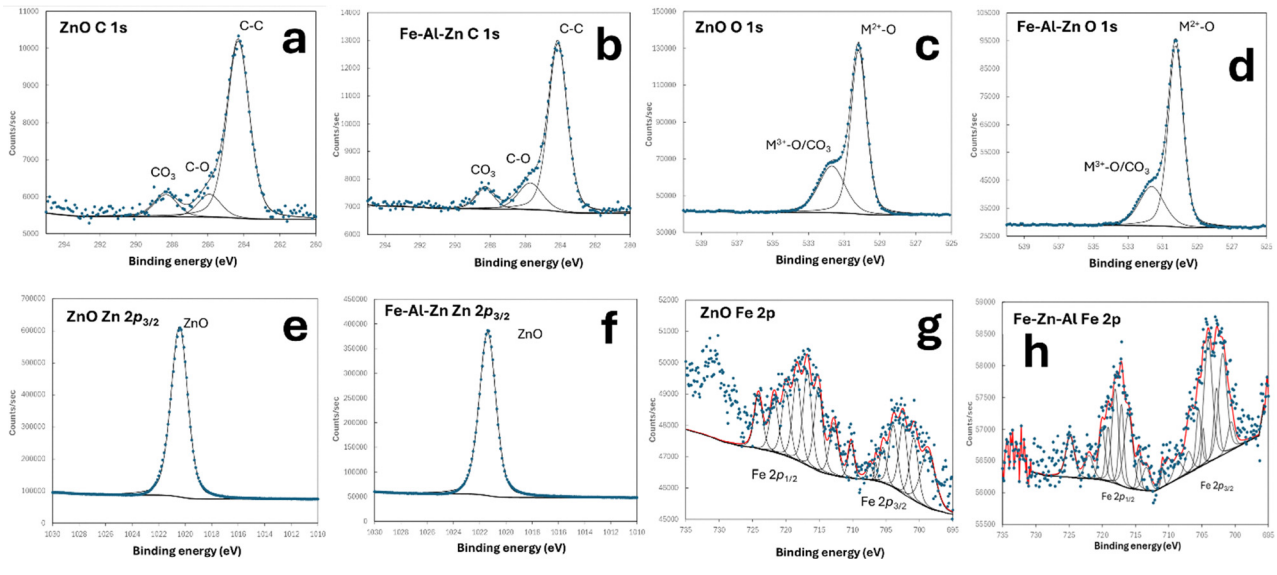

Fig. 2 High-resolution XPS spectra of ZnO and Fe–Al–ZnO samples: (a) and (b) C 1s showing C–C, C–O, and carbonate (CO_3) contributions; (c) and (d) O 1s deconvoluted into lattice oxygen (~530 eV) and higher binding energy components (~531–532 eV) associated with defect-related oxygen and surface species; (e) and (f) Zn $2p_{3/2}$ confirming Zn^{2+} in ZnO with a slight binding energy shift upon doping; (g) and (h) Fe 2p spectrum of Fe–Al–ZnO exhibiting broad multiple features consistent with Fe^{2+}/Fe^{3+} states, while the ZnO sample shows only a weak Fe signal near the detection limit.

doped sample indicates modification of the local electronic environment due to dopant incorporation and defect interactions, suggesting changes in the electronic structure.

The Fe 2p spectra of the pristine ZnO and Fe/Al co-doped ZnO sample exhibit broad and asymmetric features with multiple splitting and satellite structures characteristic of transition metal species (Fig. 2g and h). These features are qualitatively consistent with the presence of mixed Fe^{2+} and Fe^{3+} states.[51,52] However, due to the low Fe concentration, spectral noise, and binding energy shifts, reliable quantification of the oxidation states is not possible. In contrast, the Fe 2p signal in pristine ZnO is very weak and close to the detection limit and therefore is not considered significant for detailed analysis.

3.3 Morphology analysis

The surface morphology of the synthesized films deposited on FTO substrates by electrochemical deposition was examined using SEM, and particle size distributions were determined from statistical analysis of multiple SEM images using ImageJ software. The pure ZnO nanorods (Fig. 3a) exhibited a dense, vertically aligned array with a mean diameter around 220 nm, indicating highly uniform growth with a narrow size distribution. Such uniformity is commonly attributed to preferential *c*-axis growth in high-quality ZnO nanorods synthesized under controlled conditions.[53,54] Upon Al doping (Fig. 3b), the nanorod diameter slightly decreased to 210 nm, reflecting increased nucleation density and suppressed lateral growth due to the incorporation of smaller Al^{3+} ions into the Zn^{2+} lattice.[55,56] This morphological refinement enhances the surface-to-volume ratio, which could increase the density of active sites for surface reactions, potentially improving photocatalytic and PEC performance. Moreover, aluminium doping leads to reduced diameter uniformity and promotes the development of slightly sharpened nanorod tips.

In the case of Fe-doped ZnO (Fig. 3c), the nanorod diameter increased significantly to an average of approximately 735 nm, accompanied by reduced size uniformity. The rods exhibited rounded tips and a porous surface texture. This enlargement suggests that Fe^{3+} incorporation alters the growth kinetics during electrochemical deposition, promoting enhanced lateral growth and inducing lattice distortion. The formation of surface porosity is likely associated with Fe^{3+} substitution for Zn^{2+}, which introduces lattice strain, and localized defect formation during crystallization.

In contrast, Fe co-doping with Al led to a significant increase in the average nanorod diameter to $\approx$583 nm, accompanied by a broader size distribution (Fig. 3d). The incorporation of Fe^{3+} ions likely altered the growth kinetics by introducing lattice strain and modifying the local electric field during electrochemical deposition, which promoted lateral rather than axial extension of the nanorods.[46] As a result, the arrays exhibited reduced size uniformity but improved crystallinity, as indicated by their sharper hexagonal facets and well-defined edges. These structural refinements may enhance light scattering and expose more reactive crystal facets, both of which contribute to the superior PEC performance observed for the Fe-co-doped sample. Moreover, as shown in (Fig. 3e), the nanorod surfaces are densely covered with nanopores of an average diameter of approximately 75 nm, while the cross-sectional FIB-SEM image (Fig. 3f) clearly

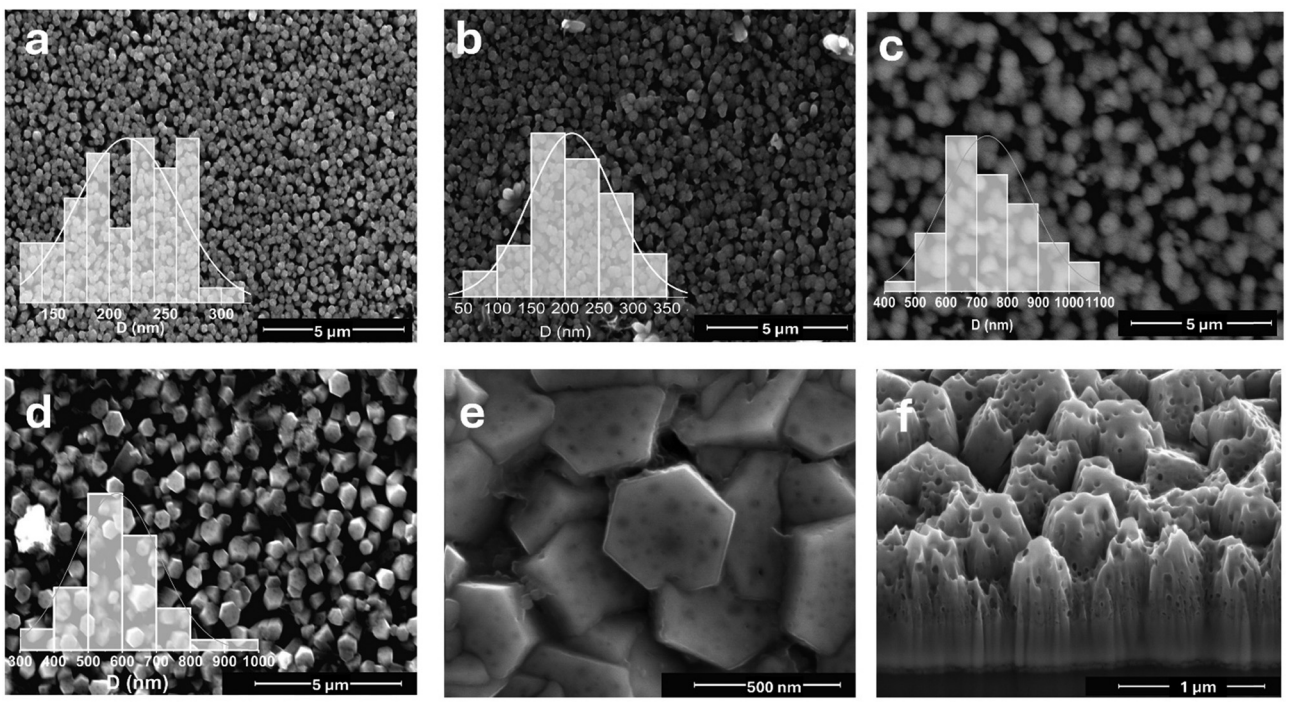

Fig. 3 SEM images of ZnO nanorods with different doping conditions: (a) pure ZnO at 5 μm scale. (b) Al-doped ZnO (AZO) at 5 μm scale. (c) Fe-doped ZnO at a 5 μm scale; (d) Al/Fe co-doped ZnO at a 5 μm scale; (e) high-magnification view at a 0.5 μm scale highlighting the nanoporous surface texture; and (f) FIB-SEM cross-section showing the porous uniformly covering the ZnO nanorods.

reveals an internally porous structure with vertically aligned rods of around 1.5 μm in length. The corresponding aspect ratio (height-to-diameter) is therefore about 2.6 : 1, indicating moderate elongation and well-ordered vertical alignment. The formation of such nanoporosity can be attributed to Fe^{3+} substitution for Zn^{2+}, which introduces lattice distortion, oxygen vacancies, and uneven growth rates, leading to the spontaneous creation of voids and channels during crystallization.

The nanoporous architecture in Al/Fe co-doped ZnO nanorods originates from dopant-induced lattice strain and defect generation during electrochemical deposition. During electrochemical deposition, the simultaneous incorporation of small radius Al^{3+} ($\approx$0.53 Å) and larger Fe^{3+} ($\approx$0.64 Å) ions into the ZnO lattice introduces competing local lattice strains.[57] Al^{3+} induces compressive distortion while Fe^{3+} causes tensile stress.[57–59] This mismatch creates microstrain fields, and might be promotes oxygen vacancy formation, and enhances defect diffusion and clustering. In particular, the substitution of Zn^{2+} by Al^{3+} or Fe^{3+} introduces excess positive charge into the lattice. Charge neutrality may be maintained *via* electron donation and/or formation of oxygen vacancies, whose formation energy can be reduced by dopant-induced lattice strain and defect interactions.[22,60,61] The vacancy formation may combine into voids and channels along grain boundaries. The presence of Al^{3+} accelerates nucleation and affects growth kinetics, causing anisotropic growth fronts and non-uniform grain coalescence.[62] The interplay of dopant stress, defect diffusion, and uneven nucleation drives the development of interconnected nanoscale porosity, which has the potential to increase effective surface area, improving light scattering, facilitating electrolyte access, and enhancing charge separation all contributing to better photoelectrochemical performance.

3.4 TEM analysis

To further elucidate the microstructure of the dual-doped ZnO nanoporous nanorods, transmission electron microscopy (TEM) analysis was performed. The thin film was mechanically scratched from the substrate and dispersed in acetone prior to TEM observation. Due to the intrinsic mechanical fragility of the highly nanoporous structure, the original nanorod morphology was partially damaged during sample preparation (Fig. S1a and b). Bright-field TEM images (Fig. S1a) show fragmented dual-doped ZnO nanorods with broken edges, exhibiting a nanoporous architecture with an average pore diameter of $\sim$50 nm. A higher-magnification image (Fig. S1b) reveals clearly distributed nanopores with sizes ranging from approximately 20 to 70 nm.

High-resolution TEM (Fig. S1c) reveals the presence of multiple crystalline domains within individual nanorods, indicating a polycrystalline structure likely arising from dopant-induced strain and enhanced nucleation during growth. Clear lattice fringes with interplanar spacings of 0.26 nm and 0.282 nm are observed, corresponding to the (002) and (100) planes of hexagonal wurtzite ZnO, respectively. A spacing of $\sim$0.52 nm, equivalent to twice the (002) interplanar distance, is also detected, further confirming *c*-axis-related crystallographic ordering. The selected area electron diffraction (SAED) pattern (Fig. S1d) exhibits concentric diffraction rings indexed to the hexagonal wurtzite ZnO phase, confirming the polycrystalline nature of the nanoporous nanorods.

3.5 Elemental mapping and dopant analysis

EDS mapping confirmed the presence and uniform distribution of Zn, O, Al, and Fe elements in the co-doped ZnO nanorods (Fig. S2a–e). The Zn map (Fig. S2b) showed slightly intense areas, likely due to variations in film thickness and surface topography or it could be local Zn-rich zones. In contrast, the O map (Fig. S1c) exhibited a highly uniform distribution, indicating of ZnO structure. Both Al and Fe maps (Fig. S1d and e) were homogeneously dispersed, verifying successful co-doping without secondary phase formation. These results verify uniform elemental incorporation and supporting the structural integrity. SEM and TEM–EDS analyses (Tables S1 and S2) confirm the successful doping of Al and Fe into the ZnO nanorods, with Zn and O as the dominant elements. The slightly Zn-rich composition may indicate possible oxygen deficiency.

To further confirm the EDS results and validate the successful incorporation of both dopants into the ZnO nanorod structure, the μ-XRF spectrum (Fig. S3a) clearly displays the characteristic emission peaks of Zn, Al, and Fe, confirming the successful incorporation of both dopants into the ZnO nanorod structure. The inset zoomed region highlights the low-energy Al Kα peak, further validating its presence within the film. Quantitative normalized μ-XRF analysis (Table S3) shows that Zn is the dominant element (78.27 at%), followed by O (20.27 at%), while Al and Fe are present at 1.06 at% and 0.40 at%, respectively, confirming successful dual doping. The corresponding elemental mapping images Fig. S3b (Zn), Fig. S3c (Al), and Fig. S3d (Fe) demonstrate that Zn is uniformly distributed across the nanorod array; the variation in colour intensity reflects thickness differences rather than compositional fluctuations. In contrast, Al and Fe exhibit a homogeneous distribution without any observable dopant aggregation or clustering, proving uniform dual-dopant incorporation throughout the nanorod film.

Elemental analysis suggests possible oxygen deficiency, which may be associated with oxygen vacancies, although other defects such as Zn interstitials or general non-stoichiometry may also contribute.[59–61,63] EDS and μ-XRF clearly confirm the presence of Al and Fe dopants, with TEM–EDS indicating a higher local dopant concentration than surface-sensitive techniques, suggesting a non-uniform dopant distribution through the film thickness. This may indicate reduced dopant concentration near the surface, possibly related to growth and conductivity changes during thickening. Such a depth-dependent dopant distribution could also explain why Al was not detected by XPS, given its surface sensitivity and the fact that the Al content is close to or below the XPS detection limit.

3.6 Optical analysis

The optical properties of the thin films were investigated using absorbance spectroscopy (300–800 nm) to evaluate their light-harvesting capabilities. Fig. 4a shows that Al/Fe doped ZnO exhibits a noticeable red shift in the absorption edge and a

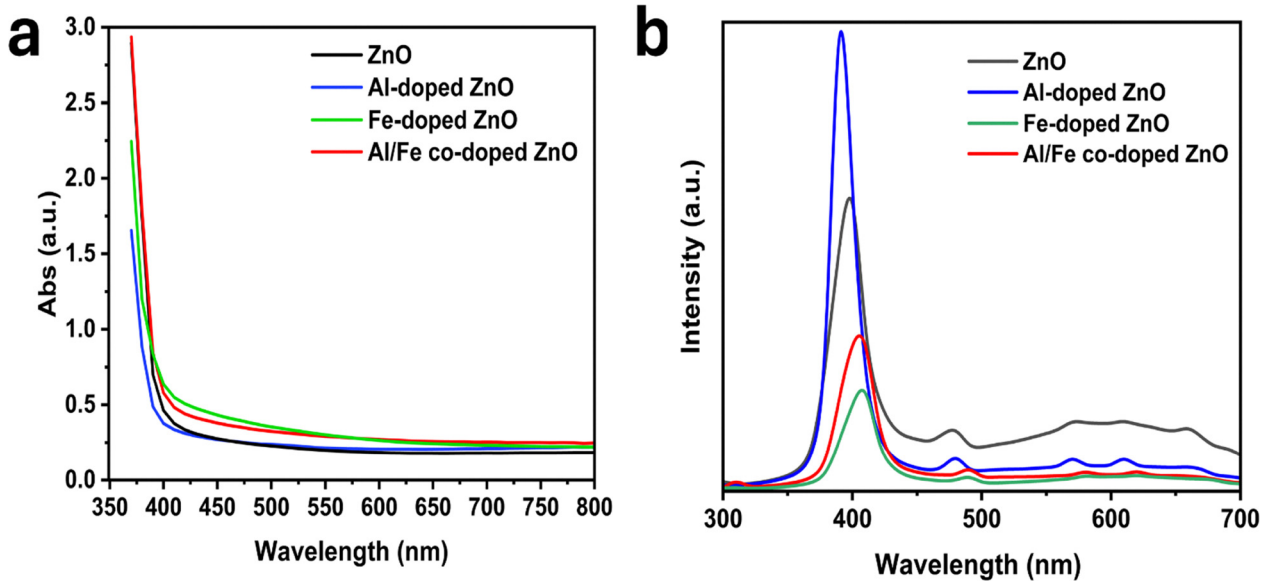

Fig. 4 (a) UV-Vis absorption spectra of pure ZnO, Al-doped ZnO, Fe-doped ZnO and Al and Fe doped ZnO thin films, showing the shift in absorption edge with doping. (b) Photoluminescence spectra of the corresponding samples recorded at room temperature with an excitation wavelength of 320 nm, illustrating changes in near-band-edge emission and defect-related deep-level emissions with doping.

modest enhancement of the absorption tail extending into the visible region compared to pristine and Al-doped ZnO. The pure ZnO thin film presents a sharp absorption at ~375 nm, corresponding to its intrinsic band gap, with strong UV absorption but limited visible-light response. Upon Al doping, the absorption edge exhibits a slight blue shift, consistent with a minor band gap widening attributed to the Burstein–Moss effect, where Al^{3+} substitution for Zn^{2+} increases free carrier concentration and partially fills the conduction band.[64] In contrast, Fe-doped ZnO and Al/Fe co-doped sample shows a red shift in the absorption edge, indicating the formation of intermediate energy states within the band gap, most likely introduced by Fe^{3+} incorporation.[65] Moreover, Fe-doped ZnO alone exhibits a slightly greater red shift than the Al/Fe co-doped film because the absence of Al-induced Burstein–Moss band filling allows Fe-related impurity and defect states to dominate, resulting in modest band-gap narrowing and enhanced visible-light absorption. These states extend the photoresponse into the visible region, while Al^{3+} simultaneously enhances carrier concentration and electrical conductivity.

Band gap values, estimated from Tauc plots derived from the absorption spectra, were found to be 3.15 eV for pure ZnO, 3.18 eV for Al-doped ZnO, 3.05 eV for Fe-doped ZnO and 3.10 eV for Al/Fe co-doped ZnO. The slight increase in band gap for AZO supports the Burstein–Moss effect, whereas the reduction for the Fe and co-doped sample is attributed to band gap renormalization and Fe^{3+} induced defect states that enhance visible-light absorption.[66]

Photoluminescence (PL) spectroscopy was employed to further investigate the electronic band structure and defect states, with spectra recorded from 300 to 700 nm at room temperature using a 320 nm excitation wavelength Fig. 4b. All samples exhibit a sharp emission near-band-edge (NBE) emission at around (400 nm) accompanied by weaker broad deep-level emissions (DLE) at visible-region (450–650 nm).

For pure ZnO, the NBE peak appears at 397 nm, corresponding to excitonic and shallow donor-related recombination in the wurtzite ZnO lattice, accompanied by a broad visible emission associated with intrinsic defects such as oxygen vacancies and zinc interstitials (Zn_i).[67,68] The slight red shift of the optical edge toward ~390–400 nm is consistent with morphology- and thickness-related effects commonly reported for ZnO nanostructures, which are attributed to structural disorder, defect-induced band tailing (Urbach states).[69] Al doping shifts the NBE to ~390 nm with significantly enhanced intensity, indicating of successful doping.[68] Al/Fe co-doping results in a red-shifted NBE at ~405 nm, in agreement with the UV-vis band gap and previous research.[66] The presence of Fe introduces intermediate or defect-states that likely facilitate absorption at lower energies.[70] This red shift is shows successfully doping of Fe counteract the Burstein–Moss blue shift typically induced by Al doping. In comparison, Fe-doped ZnO exhibits a further red shift to ~407 nm, reflecting a more pronounced influence of Fe-related defect levels on the recombination process. The visible emission intensity is notably reduced compared to pure ZnO, indicating modification of defect-related recombination pathways. While reduced PL intensity may suggest decreased radiative recombination, it can also arise from enhanced non-radiative recombination *via* deep defect states, particularly in heavily doped and defect-rich systems such as Al/Fe co-doped ZnO. The presence of residual emission in the 500–600 nm range supports the existence of deep-level defects, likely associated with Fe-related complexes or oxygen vacancies. However, the improved photocurrent and charge-transfer behavior suggest that the overall effect of these defect states is beneficial for photoelectrochemical performance.

3.7 Electrochemical impedance spectroscopy

Electrochemical impedance spectroscopy (EIS) was performed to evaluate the charge-transport behaviour of the Al/Fe doped

ZnO thin-film photoanodes, and all impedance spectra were fitted using Autolab NOVA 2.1. The Nyquist plots for pristine, Fe and Al-doped ZnO were well modelled using a standard equivalent circuit, consistent with a single interfacial charge-transfer process. In contrast, the Al/Fe doped sample under illumination required an extended two-time constant model, due to the clear presence of two semicircles.

Pristine ZnO exhibited one large semicircle, with a high charge transfer resistance of R_{ct} = 3420 Ω cm^2 (dark), decreasing to 2240 Ω cm^2 (light), reflecting sluggish interfacial kinetics and low photogenerated carrier density (Fig. 5a). Al doping moderately improved charge transport, reducing R_{ct} to = 3140 Ω cm^2 (dark) and = 1050 Ω cm^2 (light), indicating enhanced conductivity and improved interfacial charge transfer, although bulk resistance remained substantial (Fig. 5b). Fe-doped ZnO exhibited a further improvement in charge-transfer characteristics, with R_{ct} decreasing to R_{ct} to = 2900 Ω cm^2 in the dark and 220 Ω cm^2 under illumination (Fig. 5c). The Nyquist plot displayed a well-defined semicircle, indicating a predominantly single charge-transfer process with relatively uniform interfacial kinetics. The pronounced reduction in R_{ct} under light suggests enhanced photogenerated carrier separation and more efficient interfacial charge transfer compared to pristine and Al-doped samples. This improvement is attributed to Fe-induced defect states and increased carrier density, which facilitate charge transport while maintaining a comparatively homogeneous electrochemical interface.

The Al/Fe doped ZnO displayed a distinctly different impedance response. In the dark, the co-doped electrode exhibited a much lower R_{ct} = 553 Ω cm^2, significantly outperforming pristine and single-doped samples (Fig. 5d). Under illumination, two well-resolved semicircles emerged: a high-frequency bulk/space-charge resistance of R_b = 33.5 Ω cm^2, and a low-frequency interfacial charge-transfer resistance of only R_{ct} = 103 Ω cm^2 (Fig. 5e). The appearance of two semicircles confirms the activation of multiple charge-transport pathways, where Al improves bulk conductivity, while Fe introduces shallow donor states, surface defects, and nanoporosity, collectively enabling defect-assisted and catalytic charge transfer.[71]

Across the ZnO, AZO, and Al/Fe–ZnO series, the progressive decrease in series resistance and the substantial reduction in charge-transfer resistance demonstrate that dual Al/Fe doping significantly enhances both bulk charge transport and interfacial reaction kinetics. These improvements are fully consistent with the markedly higher photocurrent density and hydrogen-generation performance observed for the Al/Fe co-doped ZnO photoanode.

3.8 Mott–Schottky analysis

The electrochemical characteristics of the ZnO-based photoanodes were examined using Mott–Schottky (M–S) analysis (Fig. 6a–c). The linear regions of the ($1/C^2$) *versus* potential plots provide critical insights into the semiconductor/electrolyte interface, revealing the conductivity type, donor density (N_d), and flat-band potential (E_{fb}). It should be noted that, due to the porous nanorod morphology and defect-rich interfaces, the extracted N_d values represent apparent donor densities rather than absolute values, as non-ideal capacitance behaviour, frequency dispersion, and interfacial area

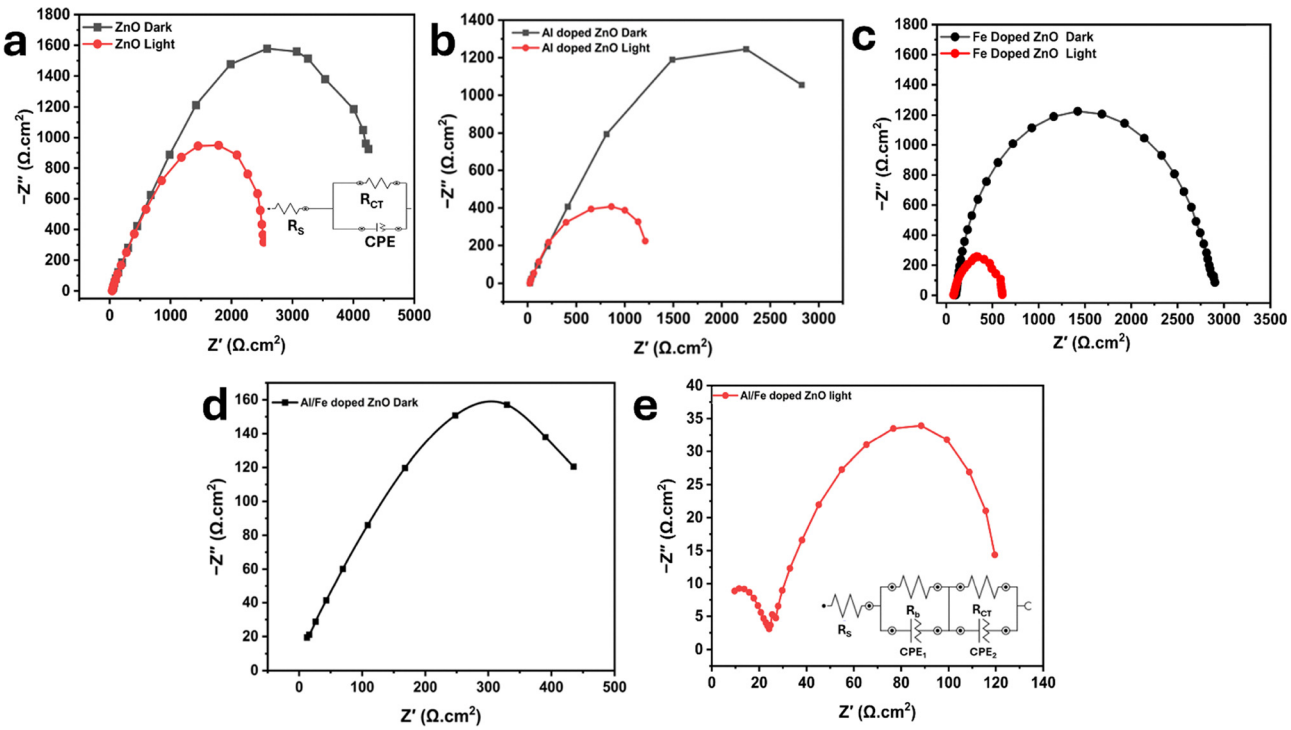

Fig. 5 Electrochemical impedance spectroscopy Nyquist plots of ZnO-based thin films under dark and light conditions. (a) Pristine ZnO under dark and light. (b) Al doped ZnO under dark and light. (c) Fe-doped ZnO under dark and light. (d) Al/Fe doped ZnO under dark conditions. (e) Al/Fe co-doped ZnO under light.

effects may contribute to the measured capacitance. In porous electrodes, the increased electrochemically active surface area is commonly described by a roughness factor (RF = $C_{dl}/C_{dl,flat}$), which may further influence the measured capacitance but is not explicitly included in the Mott–Schottky N_d calculation. All the electrodes displayed linear regions with positive slopes, confirming their n-type semiconducting behaviour, consistent with the intrinsic electronic structure of ZnO.[68]

For the undoped ZnO electrode (Fig. 6a), the M–S plot exhibited a relatively steep positive slope of 1.51×10^{12} F^{-2} V^{-1}, corresponding to a donor density of 1.1×10^{19} cm^{-3} and an E_{fb} of −0.09 V *vs.* RHE. Near result in previous research.[68,72] Al doping markedly improved the electrical properties by substituting Zn^{2+} with Al^{3+}, introducing extra conduction electrons (Fig. 6b). The slope for Al doped ZnO (AZO) decreased significantly to 1.93×10^{11} F^{-2} V^{-1}, yielding a higher donor density of 8×10^{19} cm^{-3}. The flat-band potential shifted slightly negative to −0.1 V *vs.* RHE, reflecting an upward shift in the conduction band edge, which facilitates faster electron transfer into the electrolyte. This confirms that Al incorporation enhances n-type conductivity and reduces series resistance, thereby improving charge separation and photoelectrochemical hydrogen generation efficiency.

For Fe-doped ZnO, (M–S) plot (Fig. 6c) exhibited a relatively steep positive slope of 4.04552×10^{11} F^{-2} V^{-1}, confirming its n-type semiconducting behaviour. This slope corresponds to a donor density of approximately 4.1×10^{19} cm^{-3}, indicating a substantial increase in charge carrier concentration compared to pristine ZnO. The enhanced donor density is attributed to Fe^{3+} incorporation, which introduces shallow donor states and defect levels that facilitate charge transport. In addition, the apparent flat-band potential was determined to be −0.12 V *vs.* RHE, suggesting a favourable band alignment for photoelectrochemical hydrogen generation efficiency and improved interfacial charge separation efficiency. Although Al-doped ZnO exhibits a higher donor density, Fe-doped ZnO shows a more negative flat-band potential, which may be attributed to Fe-induced defect states and possible oxygen vacancies that modify band-edge positions and interfacial energetics beyond simple carrier concentration effects.[22]

Dual doping with Al and Fe further amplified the electronic conductivity and photoactivity (Fig. 6d). It exhibited an even smaller slope of 8.82×10^{10} F^{-2} V^{-1}, corresponding to a high donor density of 1.9×10^{20} cm^{-3} and the apparent flat-band potential was −0.19 V *vs.* RHE. The co-doping introduced shallow donor states and facilitated Fe^{3+}/Fe^{2+} redox mediation, improving interfacial charge transport. The higher donor concentration and reduced space charge resistance in Al and Fe doped ZnO explain its stronger tendency for hydrogen evolution under illumination, as the Fermi level is closer to the conduction band, enabling electrons to reach potentials much below the H^+/H_2 level. Moreover, illumination caused a negative shift in the apparent flat-band potential for all samples, consistent with photo excited quasi-Fermi level movement. The FTO substrate also contributed to enhanced carrier collection, particularly under light bias, by providing a highly conductive pathway for photogenerated electrons.

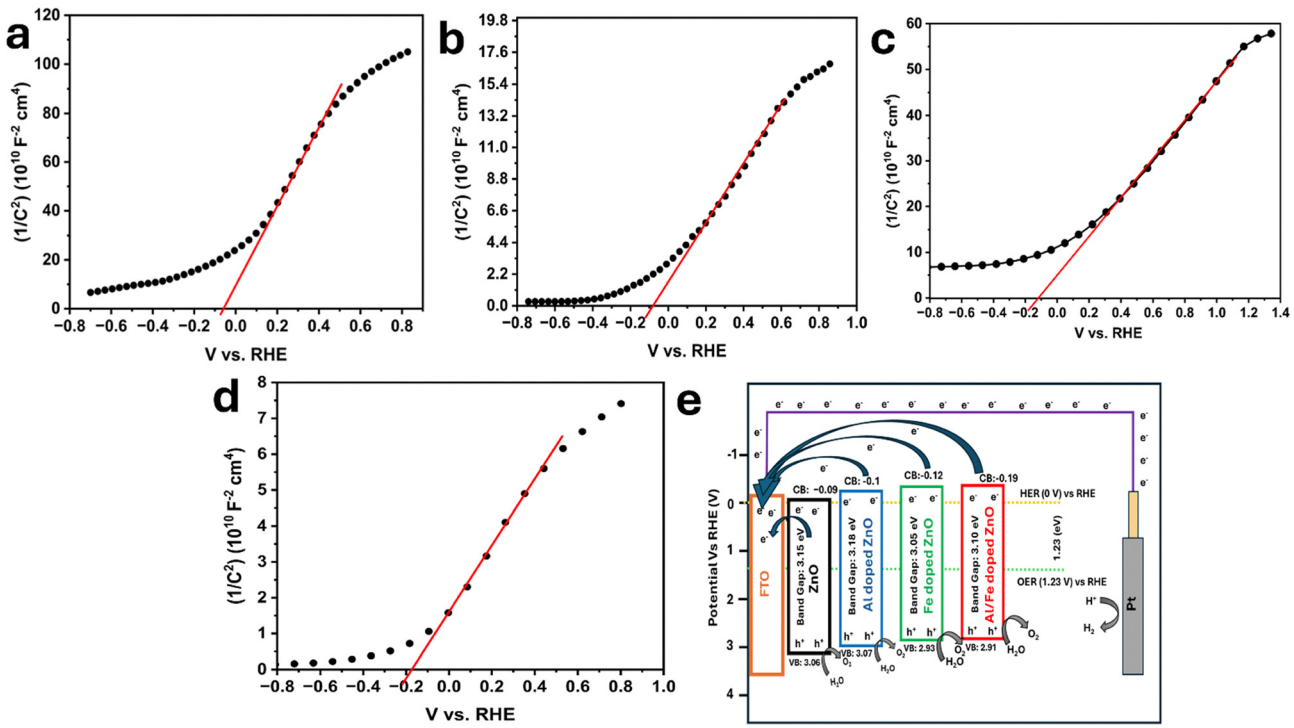

Fig. 6 Mott–Schottky plots of (a) undoped ZnO nanorods, (b) Al-doped ZnO nanorods, and (c) Fe-doped ZnO nanorods (d) Al and Fe co-doped ZnO nanorods. (e) Band edge alignment and charge transfer pathways of ZnO, Al doped ZnO, and Al and Fe doped ZnO on FTO *versus* RHE, illustrating electron extraction to platinum for HER and hole-driven OER.

3.9 Band edge alignment

Fig. 6e shows qualitative illustration of the band edge alignment of ZnO, Al doped ZnO, and Al/Fe doped ZnO photoanodes deposited on FTO substrates, plotted *versus* (RHE) at pH 9. All three ZnO-based materials possess conduction band minima (CBM) positioned more negative than the hydrogen evolution potential (0 V *vs.* RHE), while their valence band maxima (VBM) extend well beyond the oxygen evolution potential (+1.23 V *vs.* RHE) confirming full thermodynamic suitability for overall water splitting.

This enhanced performance can be attributed to several synergistic factors. First, the flat-band potentials extracted from the Mott–Schottky plots were determined to be −0.09, −0.10, −0.12, and −0.19 V *vs.* RHE for pristine ZnO, Al-doped ZnO, Fe-doped ZnO, and Al/Fe co-doped ZnO, respectively. These values serve as approximate indicators of the conduction-band edge positions. And the corresponding VBMs estimated from $E_{fb} + E_g$ (+3.06, +3.07, +3.00 and +2.91 V *vs.* RHE) represent apparent band-edge positions; these shifts arise from doping-induced modifications of the Fermi level and band bending rather than true movement of the intrinsic valence band.

Moreover, the FTO substrate, whose conduction band is positioned near +0.05 V *vs.* RHE, provides an energetically favourable pathway for electron extraction and transport to the counter electrode. Consequently, photogenerated electrons migrate efficiently from the ZnO conduction band into FTO, acquiring sufficient driving force to reduce protons at the cathode. In addition, under illumination the electron quasi-Fermi level in the semiconductor shifts toward more negative potentials, effectively increasing the reduction potential.[73] The high donor density induced by Al and Fe co-doping ensures abundant free carriers, while surface catalytic sites minimise the kinetic overpotential required for H_2 evolution.

3.10 PEC performance

The photoelectrochemical performance of ZnO, Al doped ZnO (AZO), and Al and Fe co-doped ZnO electrodes was systematically evaluated under simulated solar illumination (1 sun) in electrolytes of varying pH including NaOH (pH 14), Na_2SO_3 + Na_2S (pH 11.44), Na_2SO_3 pH 9 and Na_2SO_4 (pH 7). Potentials were measured against Ag/AgCl (3 M KCl) and converted to the RHE scale according to eqn (1).

Across all conditions, photocurrents increased significantly once the potential exceeded the threshold values. Among all samples, the Al/Fe co-doped ZnO exhibited the highest photocurrent density, reaching ∼3 mA cm^{-2} at 1 V *vs.* RHE. In comparison, Al-doped ZnO achieved ∼2.6 mA cm^{-2}, Fe-doped ZnO ∼2.5 mA cm^{-2}, and pristine ZnO ∼1.7 mA cm^{-2} (Fig. 7a). This enhancement is attributed to the synergistic effects of Al, which increases carrier density and electrical conductivity, and Fe, which introduces intermediate states that extend light absorption into the visible region, thereby improving charge separation and transfer efficiency.[73,74] Additionally, Fe incorporation promotes nanorod porosity formation, which enhances surface area, light scattering, and electrolyte penetration, significantly contributing to the improved PEC activity.[25] The doping optimization heatmap (Fig. S4) shows that Al and Fe doping enhance PEC performance up to an optimal level, while co-doping further improves performance, with the best results observed at moderate concentrations, indicating a synergistic effect at 1 V *vs.* RHE.

Among all electrolyte, the mixed solution of 75% Na_2SO_3 + 25% Na_2S (pH 11.44) shows highest photocurrent (Fig. 7b). At an applied potential of 1 V *vs.* RHE, Al and Fe co-doped ZnO electrode delivered a photocurrent density approximately four times higher in this mixed electrolyte (8.9 mA cm^{-2}) compared to Na_2SO_4 (2 mA cm^{-2}) (pH 7) and 3 times higher than Na_2SO_3 (3 mA cm^{-2}) (pH 9). NaOH shows a high current at low voltage, which might be due to high pH (pH 14). The PEC measurements in (75% Na_2SO_3 + 25% Na_2S) showed a sharp rise in photocurrent at low applied voltage, reflecting efficient hole scavenging by sulfide ions.[75] However, unlike Na_2SO_4, the current–voltage curve was not linear, displaying curved and unstable transients due to capacitive effects and side reactions. Beyond a certain potential, the photocurrent increase became very limited and reduced, indicating mass-transport and surface reaction constraints rather than voltage-driven enhancement. The most reliable indicators of true water splitting were observed in NaOH and Na_2SO_4, where the co-doped ZnO demonstrated superior performance confirming its potential as an advanced photoanode material for solar hydrogen generation.[74]

Fig. 7c shows that during illumination, visible gas bubbles were continuously generated on the surface of the platinum wire while co-doped ZnO was the photoanode, confirming active hydrogen evolution. The steady and uniform bubbling pattern indicates efficient charge transfer and stable catalytic activity throughout the reaction period. The results clearly show that electrolyte composition and doping strongly influence the photoelectrochemical response: ZnO exhibits relatively low activity, whereas Al doping enhances the current and Al and Fe co-doping deliver the highest values overall.

The stability profile of the Al and Fe doped ZnO reveals a strong dependence on electrolyte environment Fig. 7d.[75] The best-performing sample was tested at 1 V *vs.* RHE under UV-filtered illumination soluar simulator. In NaOH (pH 14), the photocurrent initially reaches nearly 6 mA but decays rapidly within the first few hundred seconds, reflecting photocorrosion processes that are well documented for ZnO under highly alkaline conditions.[16,76] By contrast, in mix of Na_2SO_3 and Na_2S (pH 11.44) the photocurrent rapidly decayed within a few seconds, and hydrogen evolution ceased after only a few minutes, indicating severe photocorrosion and instability of the electrode under sulfide rich alkaline conditions. The severe instability is observed despite the hole-scavenging nature of sulfide ions. This can be attributed to the combined effects of alkaline dissolution and possible surface reactions between Zn^{2+} and S^{2-} species, which may lead to surface reconstruction or passivation instability.

In Na_2SO_3 (pH 9), the co-doped ZnO electrode exhibited a stable photocurrent density of approximately 3.0 mA cm^{-2} over 5 h, with only minor fluctuations, demonstrating excellent operational durability under moderately alkaline conditions.

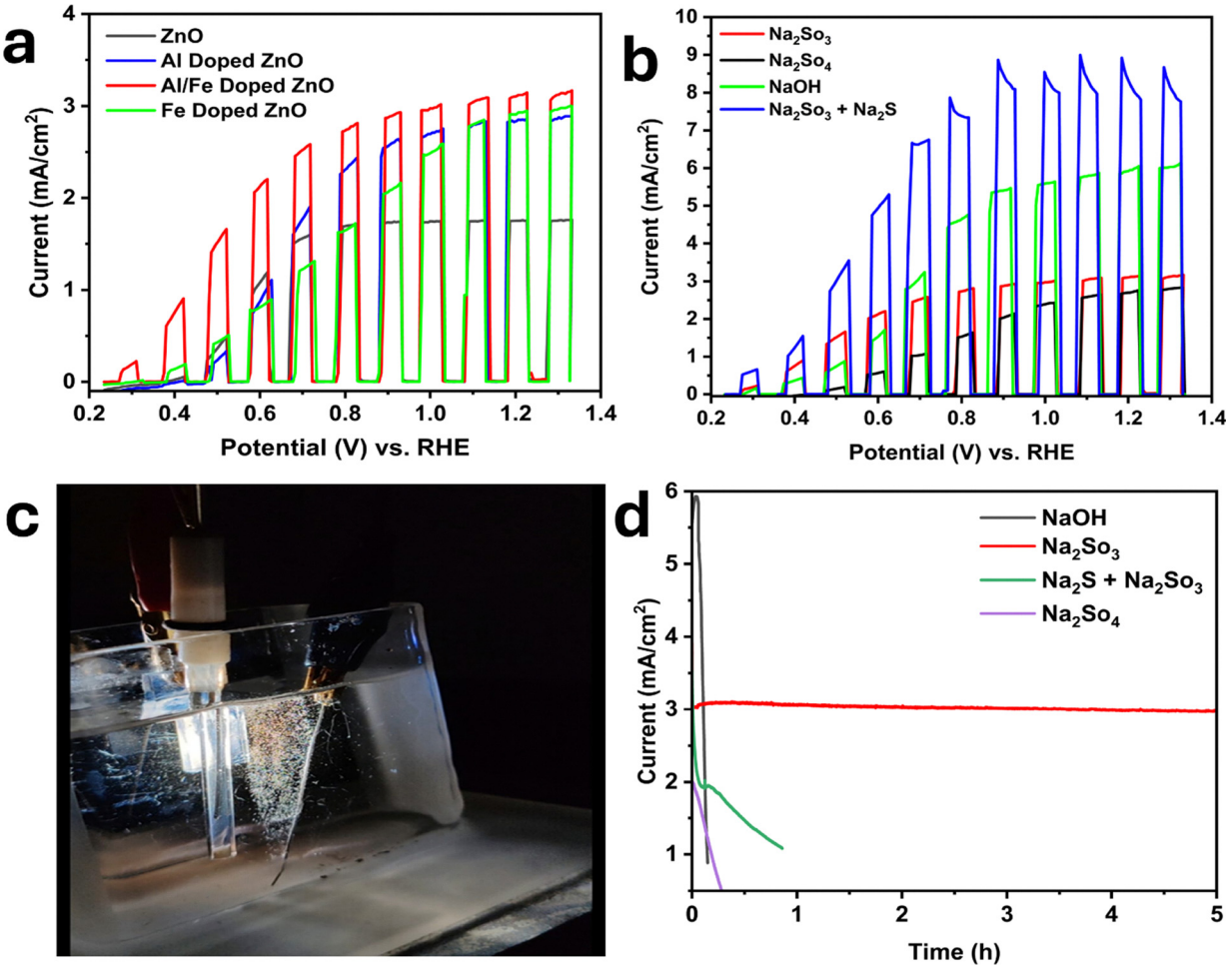

Fig. 7 Photoelectrochemical performance of (a) ZnO at different doping levels: pristine ZnO, Al-doped ZnO, Fe-doped ZnO and Al and Fe co-doped ZnO electrodes measured in Na_2SO_3 electrolyte (pH 9); (b) Al and Fe co-doped ZnO electrodes tested in various electrolytes Na_2SO_3 (pH 9), 75% Na_2SO_3 + 25% Na_2S (pH 11.44), NaOH (pH 14), and Na_2SO_4 (pH 7) under solar-simulator illumination (1 sun); (c) real photograph of the photoelectrochemical (PEC) hydrogen evolution setup. The image shows the working electrode (Al/Fe–ZnO sample), Pt wire counter electrode, and Ag/AgCl reference electrode immersed in the electrolyte under illumination, where visible hydrogen bubbles form on the photoanode surface during water splitting. (d) Life-cycle stability of Al and Fe co-doped ZnO in the same electrolytes under solar-simulator illumination (1 sun) at an applied potential of 1 V *vs.* RHE.

This stability is primarily attributed to the presence of sulfite ions, which serve as efficient hole scavengers that rapidly consume photogenerated holes, thereby suppressing photocorrosion and enabling sustained hydrogen evolution. In contrast, in Na_2SO_4 (pH 7), the faster photocurrent decay was observed, which can be attributed to hole accumulation at the ZnO surface in the absence of effective hole scavengers. Under these conditions, the decay is primarily governed by photocorrosion rather than chemical dissolution. The highly nanoporous morphology of the ZnO nanorods further accelerates this process by increasing the active surface area available for oxidative reactions.

After more than four months of intermittent photoelectrochemical operation during which the cell was repeatedly switched on and off over multiple days, the dual-doped ZnO nanorod electrode exhibited pronounced morphological degradation after a total accumulated illumination time of 24 000 s, as illustrated in Fig. 8a–f. At low magnification (Fig. 8a), extensive peeled-off regions are visible, indicating partial delamination of the nanorod film from the FTO substrate due to repeated wetting, drying, and light-induced stress. A closer view at Fig. 8b shows that the initially dense and vertically aligned nanorods have transformed into flake or feather like structures, with localized thickening and surface accumulation, suggesting dissolution reprecipitation dynamics during cyclic testing. In Fig. 8c, this transformation is more evident, as the feather-like features clearly replace the original rod geometry.

A higher magnification image (Fig. 8d) reveals that these flakes are loosely bound and fragile, confirming the mechanical weakening of the photoanode surface. Further magnification (Fig. 8e) demonstrates that the nanorods have lost their distinct hexagonal morphology, instead forming larger, roughened grains through partial merging and surface reconstruction. Finally, Fig. 8f presents the highest magnification view, highlighting the highly porous and coarse surface texture that increased after prolonged operation a clear indication of Zn^{2+} leaching and structural collapse.

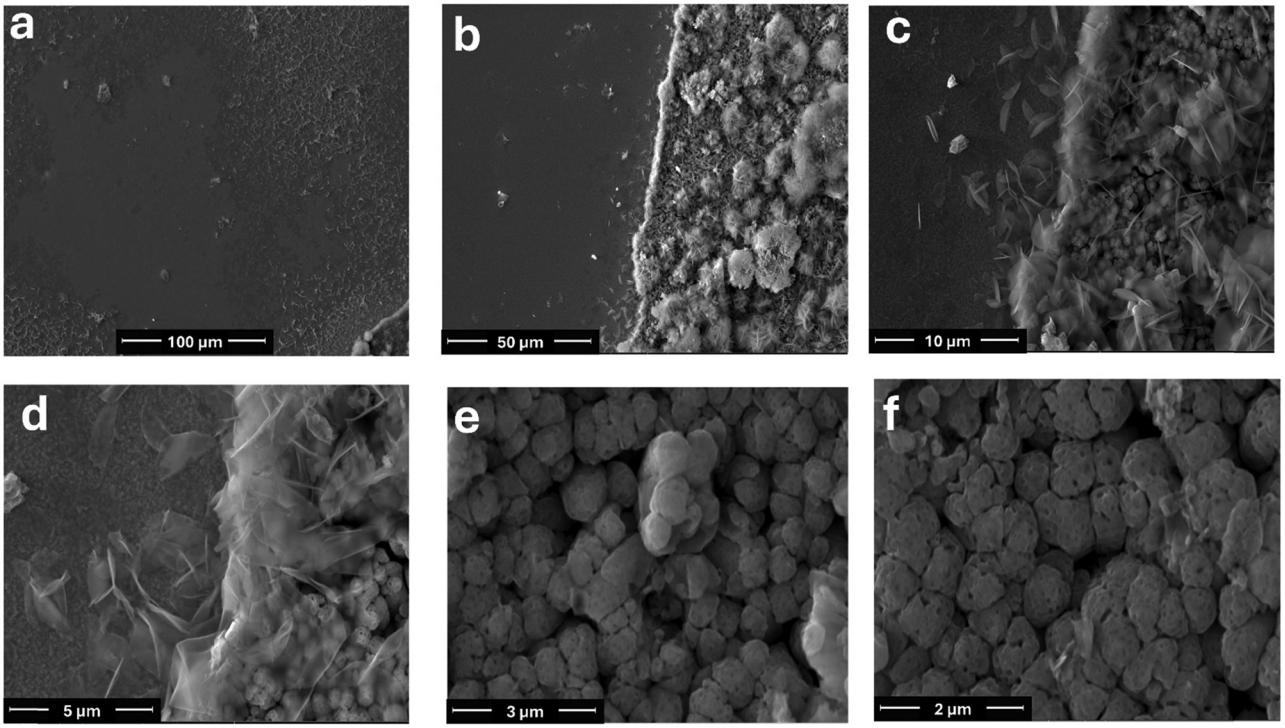

Fig. 8 SEM images of the dual-doped ZnO nanorod electrode after prolonged intermittent PEC operation (total illumination time: (24 000 s). (a) Peeled-off regions on the surface (100 μm). (b) Transformation of nanorods into flake or feather like structures (50 μm). (c) Clear conversion from rods to feather-like morphology (10 μm). (d) Loosely attached and fragile flakes on the surface (5 μm). (e) Loss of hexagonal shape and merging of adjacent rods (3 μm). (f) Porous and rough surface indicating corrosion and Zn^{2+} leaching (2 μm).

The XRD pattern recorded after 5 h of PEC operation (Fig. S5) shows the emergence of additional low-angle reflections, attributed to transient surface hydroxide or ion-associated deposits formed during electrochemical operation in Na_2SO_3 electrolyte. These peaks disappeared after rinsing/cleaning, confirming that they originate from removable surface species rather than any phase transformation of the ZnO wurtzite lattice. Moreover, the relative intensity of the (002) reflection decreased, while the (100) and (101) reflections became more pronounced, indicating a partial loss of *c*-axis preferential orientation. This behavior is consistent with surface photocorrosion and reconstruction of the vertically aligned nanorods, involving partial ZnO dissolution and subsequent re-precipitation processes during PEC testing.

TEM images (Fig. S6a and b) recorded after 5 h of PEC operation in Na_2SO_3 electrolyte (pH 9) show that the nanoporous framework becomes partially smoothed and decorated with flake-like nanostructures that still retain internal nanopores. This morphological evolution is attributed to surface photocorrosion during operation. The observed reduction in pore density is associated with surface reconstruction involving partial ZnO dissolution under applied bias, followed by re-precipitation of zinc hydroxide and zinc sulfite/sulfate species formed through sulfite adsorption and oxidation. These newly formed porous flake-like deposits partially block the original nanopores, resulting in a denser and reconstructed surface layer.

The best-performing photoanode in this study was the Al and Fe doped ZnO thin film, which delivered a photocurrent density of 3 mA cm^{-2} at 1 V *vs.* RHE and 1.6 mA cm^{-2} at just 0.5 V when tested in 0.1 M Na_2SO_3 electrolyte under solar simulator 1 sun. The high photocurrent response, together with the stability provided by this electrolyte, makes this sample electrolyte pair the optimal system for further analysis.

The Al and Fe co-doped ZnO photoelectrode developed in this work exhibits markedly superior photoelectrochemical performance compared with previously reported ZnO-based systems. For example, ZnO/Ag_2WO_4/AgBr nanorods achieved a photocurrent density around ~3 mA cm^{-2} for 1 V *vs.* RHE in Na_2SO_4 electrolyte,[77] whereas ZnO/α-Fe_2O_3 heterostructures generated ~1.1 mA cm^{-2} for 1 V *vs.* RHE in 1 M NaOH electrolyte.[78] These results clearly demonstrate the synergistic enhancement achieved through dual Al and Fe doping combined with optimized electrolyte engineering, leading to a significant improvement in charge separation and light-harvesting efficiency relative to previously reported ZnO systems.

3.11 Photocatalytic hydrogen production rates

The plotted data in Fig. 9 illustrates the time-dependent hydrogen output rate of a dual-doped ZnO thin film photoelectrode operating under 1 sun at an applied potential of 1 V *vs.* RHE in Na_2SO_3 electrolyte at pH 9. The hydrogen production rate, normalized per unit area (mL cm^{-2}), increases steadily from ~1.7 to ~5.7 mL cm^{-2} over 5 h, indicating continuous and stable photoelectrochemical activity during prolonged operation.

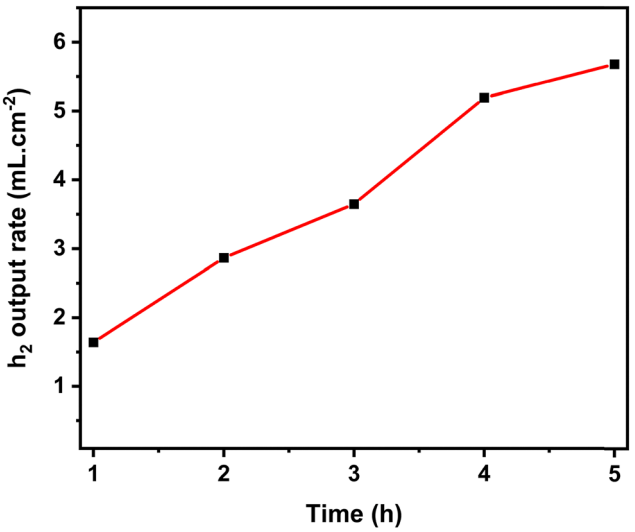

Fig. 9 Time-dependent hydrogen evolution rate (mL cm^{-2}) of dual-doped ZnO thin film under 1 sun of illumination, at 1 V bias *vs.* RHE in Na_2SO_3 electrolyte (pH 9).

This behavior reflects the beneficial effect of the dual-doping in enhancing charge carrier separation and visible-light absorption. The strong correlation between photocurrent response and hydrogen evolution provides qualitative confirmation of efficient interfacial charge transfer and stable PEC performance under visible-light illumination.

4. Conclusion

This study shows that Al and Fe co-doping provides a powerful strategy to overcome the intrinsic limitations of ZnO photoanodes for PEC water splitting. The co-doped ZnO nanorods exhibited markedly improved performance, delivering a photocurrent density of 3 mA cm^{-2} in Na_2SO_3 at 1 V *vs.* RHE under simulator solar of 1 sun illumination substantially higher than pure and single doped ZnO. Electrochemical analyses revealed favourable band alignment, reduced charge-transfer resistance, and enhanced carrier density, while electrolyte studies confirmed that pH and redox environment strongly influence onset potential and stability. Although Na_2SO_3 + Na_2S enabled high activity at low bias through efficient hole scavenging, its instability and mass-transport limitations highlighted Na_2SO_3 as a more reliable electrolyte for sustained operation. Furthermore, stable visible-light-driven hydrogen evolution of 5.7 mL cm^{-2} over 5 hours highlights the electrode's durability and efficiency under solar-relevant operation.

Structural analyses reveal that Al doping produces finer nanorods, whereas the introduction of Fe induces coarsening, increased size dispersion, and the formation of a nanoporous surface consistent with dopant-mediated lattice strain and modified growth kinetics. These morphological features are correlated with increased electroactive surface area and improved electrolyte accessibility, which are consistent with the observed enhancement in PEC performance of the dual-doped ZnO photoanodes.

Overall, the enhanced activity arises from synergistic effects of Al^{3+}-induced conductivity improvement and Fe^{3+}-related electronic states that extend light absorption and facilitate interfacial charge transfer, leading to increased photocarrier generation under solar illumination and modified recombination pathways.

Author contributions

MMRA conceptualization, data curation, formal analysis, writing original draft. AAT data curation, validation, resources, formal analysis, writing – review & editing. MS investigation, data curation, validation, review and editing.

Conflicts of interest

The authors declare no competing financial interests.

Data availability

All data supporting this study are included in the article and supplementary information (SI). Supplementary information is available. See DOI: https://doi.org/10.1039/d5ya00362h.

Additional raw datasets are available from the corresponding author upon reasonable request.

Acknowledgements

MMRA acknowledges the Higher Committee of Education Development (HCED), Government of Iraq, for his PhD grant. A. A. T. would like to acknowledge the Engineering and Physical Sciences Research Council (EPSRC), UK, under research grant numbers UKRI647. The authors thank the Critical Minerals Equipment Hub (CMEH) at the Camborne School of Mines, University of Exeter, for providing access to micro-XRF systems used in the analysis of the samples in this research.

References

1 United Nations (2022) World Population Prospects 2022. Department of Economic and Social Affairs, Population Division, https://population.un.org/wpp/, (accessed 7/9, 2025).
2 IEA (2021) World Energy Outlook 2021. International Energy Agency, https://www.iea.org/reports/world-energy-outlook-2021, (accessed 07/09, 2025).
3 IPCC (2023) Climate Change 2023: Synthesis Report. Intergovernmental Panel on Climate Change, https://www.ipcc.ch/report/sixth-assessment-report-cycle/).
4 J. Incer-Valverde, A. Korayem, G. Tsatsaronis and T. Morosuk, *Energy Convers. Manage.*, 2023, **291**, 117294.
5 A. Ajanovic, M. Sayer and R. Haas, *Int. J. Hydrogen Energy*, 2022, **47**, 24136–24154.
6 A. Jilani and H. Ibrahim, *Energies*, 2025, **18**, 1603.
7 J. Talibawo, S. Nasejje and W. Ochen, *Nano Sel.*, 2025, e70032.

8 M. Kumar, B. Meena, P. Subramanyam, D. Suryakala and C. Subrahmanyam, *NPG Asia Mater.*, 2022, **14**, 88.
9 T. R. Harris-Lee, F. Marken, C. L. Bentley, J. Zhang and A. L. Johnson, *EES Catal.*, 2023, **1**, 832–873.
10 A. A. Mohd Raub, R. Bahru, S. N. A. Mohd Nashruddin and J. Yunas, *Heliyon*, 2024, **10**, e39079.
11 M. Ma, Y. Huang, J. Liu, K. Liu, Z. Wang, C. Zhao, S. Qu and Z. Wang, *J. Semicond.*, 2020, **41**, 091702.
12 H. Eidsvåg, S. Bentouba, P. Vajeeston, S. Yohi and D. Velauthapillai, *Molecules*, 2021, **26**(6), 1687.
13 J. K. Cooper, S. Gul, F. M. Toma, L. Chen, Y.-S. Liu, J. Guo, J. W. Ager, J. Yano and I. D. Sharp, *J. Phys. Chem. C*, 2015, **119**, 2969–2974.
14 M. M. R. Al-Fartoos, A. Roy, T. K. Mallick and A. A. Tahir, *Commun. Eng.*, 2024, **3**, 145.
15 D. Bakranova and D. Nagel, *Clean Technol.*, 2023, **5**, 1248–1268.
16 M. I. Dagareh, H. Y. Hafeez, J. Mohammed, A. D. G. Kafadi, A. B. Suleiman and C. E. Ndikilar, *Chem. Phys. Impact*, 2024, **9**, 100774.
17 A. Janotti and C. G. Van de Walle, *Rep. Prog. Phys.*, 2009, **72**, 126501.
18 H. R. Khan, M. Aamir, B. Akram, M. A. Malik, A. A. Tahir, M. A. Choudry and J. Akhtar, *Bull. Mater. Sci.*, 2022, **45**, 55.
19 A. A. Aboud, M. Shaban and N. Revaprasadu, *RSC Adv.*, 2019, **9**, 7729–7736.
20 H. R. Khan, B. Akram, M. Aamir, M. A. Malik, A. A. Tahir, M. A. Choudhary and J. Akhtar, *Sci. Rep.*, 2020, **10**, 9707.
21 D. Dridi, L. Bouaziz, M. Karyaoui, Y. Litaiem and R. Chtourou, *J. Mater. Sci.: Mater. Electron.*, 2018, **29**, 8267–8278.
22 S. Banerjee, S. Padhan and R. Thangavel, *Mater. Chem. Phys.*, 2022, **277**, 125548.
23 S. Bimli, S. R. Mulani, E. Choudhary, A. Miglani, P. Shinde, S. R. Jadkar, R. J. Choudhary and R. S. Devan, *Int. J. Hydrogen Energy*, 2024, **71**, 227–238.
24 A. Hussain, S. Fiaz, A. Almohammedi and A. Waqar, *Heliyon*, 2024, **10**, e35725.
25 H. R. Khan, M. Aamir, B. Akram, A. A. Tahir, M. A. Malik, M. A. Choudhary and J. Akhtar, *Mater. Res. Bull.*, 2020, **122**, 110627.
26 C. H. Kalyani, I. V. Subba Reddy, P. Raju and P. Missak Swarup Raju, *Mater. Today: Proc.*, 2023, **80**, 1111–1115.
27 O. Akhavan, *ACS Nano*, 2010, **4**, 4174–4180.
28 X. Zhang, J. Qin, Y. Xue, P. Yu, B. Zhang, L. Wang and R. Liu, *Sci. Rep.*, 2014, **4**, 4596.
29 M. R. Almamari, N. M. Ahmed, A. M. Holi, F. K. Yam, H. H. Kyaw, M. A. Almessiere and M. Z. Al-Abri, *Materials*, 2022, **15**(17), 5827.
30 M. Bakry, W. Ismail, M. Abdelfatah and A. El-Shaer, *Sci. Rep.*, 2024, **14**, 23788.
31 U. Naz, J. Ambreen, A. Mumtaz, H. Sajid, S. Sardar, S. Khan, S. Saidin, M. R. Hatshan and M. Khan, *Mater. Sci. Eng., B*, 2025, **321**, 118568.
32 L. Yan, W. Zhao and Z. Liu, *Dalton Trans.*, 2016, **45**, 11346–11352.
33 D. Maity, K. Karmakar, D. Mandal, D. Pal, G. G. Khan and K. Mandal, *Nanotechnology*, 2020, **31**, 475403.
34 R. Wang, C. Chen, Y. Kan, W. Fang, X. Li, L. Wang and Y. Jia, *J. Electroanal. Chem.*, 2025, **976**, 118790.
35 A. S. S. Bilal, M. U. A. Khan, N. Banik, A. Hayitov, R. MM, S. Ray, K. Ghai, U. Singh, E. Khudoynazarov and M. Aleem, *J. Mater. Sci.: Mater. Eng.*, 2025, **20**, 104.
36 I. Ahmad, M. Mazhar, M. Usmani, K. Khan, S. Ahmad and J. Ahmad, *J. Ovonic Res.*, 2019, **15**(1), 1–13.
37 C.-F. Liu, Y.-J. Lu and C.-C. Hu, *ACS Omega*, 2018, **3**, 3429–3439.
38 M. Fekete, W. Riedel, A. F. Patti and L. Spiccia, *Nanoscale*, 2014, **6**, 7585–7593.
39 A. Galdámez-Martínez, Y. Bai, G. Santana, R. S. Sprick and A. Dutt, *Int. J. Hydrogen Energy*, 2020, **45**, 31942–31951.
40 F. Abrinaei, *J. Mater. Sci.: Mater. Electron.*, 2019, **30**, 8619–8628.
41 J. L. van Heerden and R. Swanepoel, *Thin Solid Films*, 1997, **299**, 72–77.
42 S. T. Khlayboonme and W. Thowladda, *Mater. Res. Express*, 2021, **8**, 076402.
43 A. Yildiz, H. Cansizoglu and T. Karabacak, *Appl. Surf. Sci.*, 2015, **352**, 2–4.
44 A. K. Mishra and D. Das, *Mater. Sci. Eng., B*, 2010, **171**, 5–10.
45 M. J. Akhtar, H. A. Alhadlaq, A. Alshamsan, M. A. Majeed Khan and M. Ahamed, *Sci. Rep.*, 2015, **5**, 13876.
46 L. Xu and X. Li, *J. Cryst. Growth*, 2010, **312**, 851–855.
47 G. Greczynski and L. Hultman, *Appl. Surf. Sci.*, 2022, **606**, 154855.
48 Table of Elements, Thermo Fisher Scientific – UK, https://www.thermofisher.com/uk/en/home/materials-science/learning-center/periodic-table/non-metal/oxygen.html, (accessed 13/04, 2026).
49 A. Senthamizhan, B. Balusamy, Z. Aytac and T. Uyar, *CrystEngComm*, 2016, **18**, 6341–6351.
50 J. Wang, D. N. Mueller and E. J. Crumlin, *J. Eur. Ceram. Soc.*, 2024, **44**, 116709.
51 M. C. Biesinger, B. P. Payne, A. P. Grosvenor, L. W. Lau, A. R. Gerson and R. S. C. Smart, *Appl. Surf. Sci.*, 2011, **257**, 2717–2730.
52 A. Grosvenor, B. Kobe, M. C. Biesinger and N. McIntyre, *Surf. Interface Anal.*, 2004, **36**, 1564–1574.
53 S. Baruah and J. Dutta, *Sci. Technol. Adv. Mater.*, 2009, **10**, 013001.
54 M. Skompska and K. Zarębska, *Electrochim. Acta*, 2014, **127**, 467–488.
55 A. Henni, A. Merrouche, L. Telli and A. Karar, *J. Electroanal. Chem.*, 2016, **763**, 149–154.
56 K. Govatsi, G. Syrrokostas, S. N. Yannopoulos and S. G. Neophytides, *Electrochim. Acta*, 2021, **392**, 138995.
57 R. D. Shannon, *Found. Crystallogr.*, 1976, **32**, 751–767.
58 K. Al-Heuseen and M. K. Alquran, *Int. J. Nanomater. Chem.*, 2017, **3**, 27–31.
59 A. Samavati, Z. Samavati, A. Ismail, M. Othman, M. A. Rahman, A. Zulhairun and I. Amiri, *RSC Adv.*, 2017, **7**, 35858–35868.
60 R. G. S. Pala and H. Metiu, *J. Phys. Chem. C*, 2007, **111**, 8617–8622.

61 C. Gao, X. Wang, H. Yang, F. Zhou, Y. Zheng, Z. Wu and Q. Zhang, *Comput. Mater. Sci.*, 2024, **240**, 112981.
62 M. C. Jun, S. U. Park and J. H. Koh, *Nanoscale Res. Lett.*, 2012, **7**, 639.
63 G. R. Dillip, A. N. Banerjee, V. C. Anitha, B. Deva Prasad Raju, S. W. Joo and B. K. Min, *ACS Appl. Mater. Interfaces*, 2016, **8**, 5025–5039.
64 C.-H. Zhai, R.-J. Zhang, X. Chen, Y.-X. Zheng, S.-Y. Wang, J. Liu, N. Dai and L.-Y. Chen, *Nanoscale Res. Lett.*, 2016, **11**, 407.
65 C. P. Rajan, N. Abharana, S. N. Jha, D. Bhattacharyya and T. T. John, *J. Phys. Chem. C*, 2021, **125**, 13523–13533.
66 C. Wang, Z. Chen, Y. He, L. Li and D. Zhang, *Appl. Surf. Sci.*, 2009, **255**, 6881–6887.
67 F. Jamali-Sheini and R. Yousefi, *Ceram. Int.*, 2013, **39**, 3715–3720.
68 F. Ghahramanifard, A. Rouhollahi and O. Fazlolahzadeh, *Superlattices Microstruct.*, 2018, **114**, 1–14.
69 R. S. Mohar, S. Iwan, D. Djuhana, C. Imawan, A. Harmoko and V. Fauzia, *AIP Conf. Proc.*, 2016, **1729**, 020024.
70 A. K. Behera, N. Mohapatra and S. Chatterjee, *J. Nanosci. Nanotechnol.*, 2014, **14**, 3667–3672.
71 J. Jian, R. Kumar and J. Sun, *ACS Appl. Energy Mater.*, 2020, **3**, 10408–10414.
72 S. Sharma, S. Singh and N. Khare, *Int. J. Hydrogen Energy*, 2016, **41**, 21088–21098.
73 S. Suo, C. Sheehan, F. Zhao, L. Xiao, Z. Xu, J. Meng, T. E. Mallouk and T. Lian, *J. Am. Chem. Soc.*, 2023, **145**, 14260–14266.
74 M. Zayed, M. A. Ghanem, M. Taha, H. A. Elsayed, A. Mehaney, M. Shaban, K. M. Mohammed and A. M. Ahmed, *J. Saudi Chem. Soc.*, 2023, **27**, 101750.
75 R. Abdullah, A. A. Jalil, M. Asmadi, N. S. Hassan, M. B. Bahari, M. Alhassan, N. M. Izzudin, M. H. Sawal, R. Saravanan and H. Karimi-Maleh, *Int. J. Hydrogen Energy*, 2025, **107**, 183–207.
76 D. Dworschak, C. Brunnhofer and M. Valtiner, *ACS Appl. Mater. Interfaces*, 2020, **12**, 51530–51536.
77 E. Mustafa, R. E. Adam, P. Rouf, M. Willander and O. Nur, *Nanoscale Res. Lett.*, 2021, **16**, 133.
78 Y.-K. Hsu, Y.-C. Chen and Y.-G. Lin, *ACS Appl. Mater. Interfaces*, 2015, **7**, 14157–14162.